Viscoelastic characterization of dispersive media by inversion of a general wave propagation model in optical coherence elastography

Fernando Zvietcovich*[a], Jannick P. Rolland[b,c], Emma Grygotis[d], Sarah Wayson[c], Maria Helguera[e], Diane Dalecki[c], and Kevin J. Parker[a,c]

[a]University of Rochester, Department of Electrical and Computer Engineering, Rochester, New York, USA, NY 14627; [b]University of Rochester, The Institute of Optics, Rochester, New York, USA, NY 14627; [c]University of Rochester, Department of Biomedical Engineering, Rochester, New York, USA, NY 14627; [d]University of Rochester, Department of Pharmacology and Physiology, Rochester, New York, USA, NY 14627; [e]Instituto Tecnológico José Mario Molina Pasquel y Henríquez, Lagos de Moreno, México, 47480

ABSTRACT

Determining the mechanical properties of tissue such as elasticity and viscosity is fundamental for better understanding and assessment of pathological and physiological processes. Dynamic optical coherence elastography uses shear/surface wave propagation to estimate frequency-dependent wave speed and Young's modulus. However, for dispersive tissues, the displacement pulse is highly damped and distorted during propagation, diminishing the effectiveness of peak tracking approaches. The majority of methods used to determine mechanical properties assume a rheological model of tissue for the calculation of viscoelastic parameters. Further, plane wave propagation is sometimes assumed which contributes to estimation errors. To overcome these limitations, we invert a general wave propagation model which incorporates (1) the initial force shape of the excitation pulse in the space-time field, (2) wave speed dispersion, (3) wave attenuation caused by the material properties of the sample, (4) wave spreading caused by the outward cylindrical propagation of the wavefronts, and (5) the rheological-independent estimation of the dispersive medium. Experiments were conducted in elastic and viscous tissue-mimicking phantoms by producing a Gaussian push using acoustic radiation force excitation, and measuring the wave propagation using a swept-source frequency domain optical coherence tomography system. Results confirm the effectiveness of the inversion method in estimating viscoelasticity in both the viscous and elastic phantoms when compared to mechanical measurements. Finally, the viscoelastic characterization of collagen hydrogels was conducted. Preliminary results indicate a relationship between collagen concentration and viscoelastic parameters which is important for tissue engineering applications.

Keywords: Elastography, viscoelasticity, cylindrical waves, optical coherence tomography, shear waves, surface acoustic waves, viscoelastic phantoms.

1. INTRODUCTION

The bio-mechanical properties of tissue such as elasticity and viscosity are fundamental properties of normal and pathological tissues.[1,2] In this regard, optical coherence tomography-based elastography (OCE) offers the possibility of a non-invasive, high-resolution, and high-contrast measurement of tissue biomechanical properties.[3,4] Dynamic OCE techniques use short-duration pulses produced by a selected excitation source in order to produce mechanical wave propagation in the tissue being studied.[5] By tracking the propagating wave, Young's modulus and other biomechanical parameters can be calculated based on the estimation of the wave speed and the selection of the correct wave propagation model dictated by the boundary conditions of the sample.[6]

The estimation of viscous parameters in addition to the classic elastic modulus is of great interest since it can provide of useful information in disease diagnosis.[8,9] Unfortunately, in many dispersive lossy tissues, propagation of shear or surface waves is rapidly damped and distorted, complicating the attempts of estimating wave speed using typical methodologies such as peak tracking.[7]

*fzvietco@ur.rochester.edu; phone 1 585 275-5069; odalab-spectrum.org/Rochester/

In OCT, some work has been done for the viscoelastic measurement of tissue assuming a rheological model.[10-13] In most of these studies, frequency-dependent wave speed measurements are fitted to theoretical models of dispersion (rheological models), disregarding valuable information given by the wave attenuation process. Therefore, the use of model-independent approaches for the viscoelastic characterization of tissue is an important trending topic in elastography since it can provide accurate intrinsic information without assumptions regarding the tissue mechanical behavior, which is in many cases unknown.

Some model-independent approaches have been proposed for ultrasound elastography,[7,14-16] and OCE.[17,18] While these approaches calculate viscoelastic properties of tissue without using a rheological model, some assumptions made may produce biased results. For example, in Schmitt et al.,[14] the plane wave assumption can be difficult to satisfy for most of the excitation methods. Also, Nenadic et al.,[15] Kazemirad et al.,[16] and Leartprapun et al.,[17] assume that waves will be observed in the asymptotic range far from the excitation source which may not be possible if the wave is highly attenuated by dispersive lossy media. Finally, Parker and Baddour[7] investigated the propagation of a cylindrical axisymmetric Gaussian shear wave in a viscoelastic media by proposing a full analytical model-independent solution that takes a first-order approach to dispersion.

In this paper, we invert a general wave propagation model following the approach of Zvietcovich et al.,[18] that incorporates space-time propagation, decay, and distortion of pulses in a dispersive medium in order to accurately estimate the elastic and viscous components of such media. The model contemplates the initial shape of the acoustic radiation force (ARF) push in space and time and uses a general first-order approximation of dispersion, avoiding the use of any particular rheological model of tissue. Experiments were conducted in elastic and viscoelastic tissue-mimicking phantoms by producing a Gaussian push using ARF excitation, and measuring the surface wave propagation using a Fourier domain optical coherence tomography (FD-OCT) system. Results from the inversion method were compared to mechanical measurements (MM) for validation. Finally, a preliminary experiment in collagen hydrogels was performed in order to confirm the validity of our approach for tissue engineering and regenerative medicine applications.

2. THEORY

2.1 Gaussian shear pulse propagation in an infinite medium

The governing equation in cylindrical coordinates for the propagation of a Gaussian shear pulse in a viscoelastic medium produced by an ultrasound (US) based ARF excitation is described as[19]

$$\nabla^2 u_z(r,t) - \frac{1}{c^2}\frac{\partial^2 u_z(r,t)}{\partial t^2} = -F_z(r)T(t), \tag{1}$$

where $r = (x^2 + y^2)^{1/2}$, as shown in Figure 1a, u_z is the displacement of the shear wave in the z-direction; c is the velocity of the shear wave; $F_z(r)$ is the applied body force proportional to the ARF beam; and $T(t)$ is the temporal application, which we will take as a rectangular function of duration a delayed $a/2$, $\text{rect}(\frac{t}{a} - \frac{1}{2})$.

Applying the Hankel transform $\mathbf{H}$ in space, and the non-unitary angular frequency Fourier transform $\mathfrak{F}$ in time to Equation 1 in cylindrical coordinates yields

$$-\varepsilon^2 \hat{U}(\varepsilon,\omega) + \frac{\omega^2}{c^2}\hat{U}(\varepsilon,\omega) = -\hat{F}(\varepsilon)\hat{T}(\omega), \tag{2}$$

where $\hat{U}(\varepsilon,\omega) = \mathfrak{F}\{\mathbf{H}\{u_z(r,t)\}(\varepsilon,t)\}(\varepsilon,\omega)$, ε is the spatial frequency, ω is the temporal angular frequency, $\hat{F}(\varepsilon) = \mathbf{H}\{F_z(r)\}(\varepsilon)$, and $\hat{T}(\omega) = \mathfrak{F}\{T(t)\}(\omega)$. Then, isolating $\hat{U}(\varepsilon,\omega)$ in Equation 2, applying the inverse Hankel transform using Baddour's theorem,[20] and selecting the appropriate solution according to the Sommerfeld radiation condition we obtain

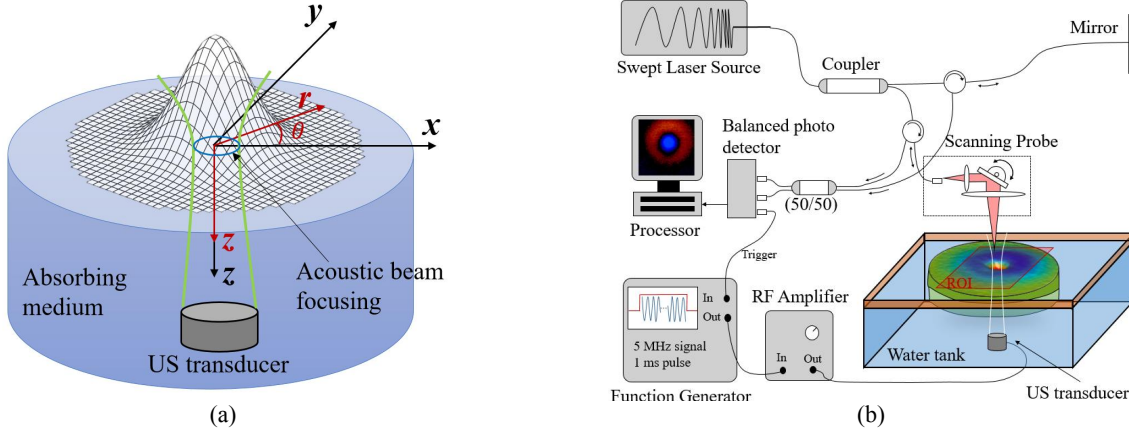$$\hat{u}(r,\omega) = -\frac{\pi i}{2}H_0^{(2)}(kr)\,\hat{F}(k)\hat{T}(\omega), \tag{3}$$

Figure 1. (a) Schematic of a Gaussian-shaped pulse produced in a dispersive medium by an ultrasound ARF transducer. The center of the pulse is the origin for the Cartesian and cylindrical coordinate system. (b) Experimental setup: PhS-OCT system implemented with a swept-source laser for motion detection.

where k is the complex wave number $k = \frac{\omega}{c} - i\alpha$, α is the absorption coefficient, and $H_0^{(2)}(x)$ is a Hankel function of the second kind. We assume that the application force $F_z(r)$ has a Gaussian beam pattern shape that is applied for a transient time a in the media. Then, the spatial Hankel and temporal Fourier transforms of $F_z(r)T(t)$ are given by

$$\hat{F}(k)\hat{T}(\omega) = \left[A_0 e^{-\sigma^2 k^2}\right]\left[e^{-\frac{i\omega a}{2}}\text{sinc}(\frac{\omega a}{2\pi})\right], \tag{4}$$

where A_0 is the force amplitude; σ is related to the curve width of the ARF Gaussian shape, and $\text{sinc}(x) = \frac{\sin(\pi x)}{\pi x}$. We are interested in finding the analytic solution of Equation 3 for particle velocity $\hat{v}(r, \omega) = i\omega\hat{u}(r, \omega)$. Then, using Equations 3 and 4, we have

$$\hat{v}(r, \omega) = A_0 \frac{\pi\omega}{2} H_0^{(2)}(kr) e^{-\sigma^2 k^2} e^{-\frac{i\omega a}{2}}\text{sinc}(\frac{\omega a}{2\pi}), \tag{5}$$

which is a closed-form analytical solution in the r-ω space that describes the cylindrical spreading of the pulsed wave, attenuation, and dispersion when it propagates through a viscoelastic medium. Given the uncertainties in choosing an appropriate rheological model, we seek a general solution that is mechanism-independent. Therefore, we introduce a first-order Taylor approximation of the frequency-dependent phase speed c and attenuation α of the wave such that

$$c \equiv c_0 + c_1 \cdot |\omega| \quad \text{and} \quad \alpha \equiv \alpha_1 \cdot |\omega|, \tag{6}$$

where $c_0 \gg c_1\omega$. Therefore, the complex frequency-dependent wavenumber will be described as

$$k(\omega) = \frac{\omega}{c_0 + c_1|\omega|} - i\alpha_1|\omega|. \tag{7}$$

For further notation simplification, we use $k'(\omega) = \frac{\omega}{c_0 + c_1|\omega|}$, and $k''(\omega) = \alpha_1|\omega|$. In a linear and isotropic viscoelastic material, the complex shear modulus $G^*(\omega) = G'(\omega) + iG''(\omega)$, where $G'(\omega)$ is the shear storage, and $G'(\omega)$ is the loss moduli, can be obtained using the real and imaginary parts of the wavenumber in Equation 7 as[21]

$$G'(\omega) = \rho\omega^2 \frac{k'(\omega)^2 - k''(\omega)^2}{(k'(\omega)^2 + k''(\omega)^2)^2}, \tag{8a}$$

$$G''(\omega) = 2\rho\omega^2 \frac{k'(\omega)k''(\omega)}{(k'(\omega)^2 + k''(\omega)^2)^2}, \tag{8b}$$

where ρ is the density of the material.

2.2 Shear to surface acoustic wave relationship

The model described in Section 2.1 was conceived for shear wave propagation. However, if we consider a semi-infinite solid medium, the predominant surface acoustic wave (SAW) propagating in the solid-vacuum interface are Rayleigh waves.[22] The relationship between shear wave and Rayleigh wave phase speed in a linear isotropic medium for a Poisson's ratio $\nu \approx 0.5$ is given by[23]

$$c \approx 1.05 * c_{\text{Rayleigh}}. \tag{9}$$

Moreover, Rayleigh waves from a point source follow cylindrical spreading $1/\sqrt{kr}$ as described in Viktorov,[23] which is consistent with the asymptotic form of the Hankel term in Equation 5, $\left|H_0^{(2)}(kr)\right| \cong \sqrt{\frac{2}{\pi kr}}$, for complex values of k.[24] Therefore, making the adjustment for phase speed as described in Equation 9, the shear wave model of Equation 5 is suitable for describing the Rayleigh wave propagation.

3. MATERIALS AND METHODS

3.1 Experimental setup

The experimental setup is shown in Figure 1b. A 5 MHz confocal ultrasonic transducer (PIM7550-2inchFL, Dakota Ultrasonics, Scotts Valley, CA, USA) with 5.01 cm of focal length was excited with a 1 ms sinusoidal tone of 5 MHz provided by a function generator (AFG320, Tektronix, Beaverton, OR, USA). The generator was connected to a RF power amplifier (25A250, Amplifier Research, Souderton, PA, USA) in order to produce an approximate Gaussian radially symmetric ($\sigma = 0.338$ mm) focused ARF push within the sample at the air-solid surface interface. The ultrasonic transducer was coupled to the sample with saline water. A phase-sensitive optical coherence tomography (PhS-OCT) system implemented with a swept source laser (HSL-2100-WR, Santec, Aichi, Japan) (center wavelength 1318 nm) was used to acquire 3D motion frames of the sample within a region of interest (ROI) of 10×10 mm in the xy-plane, and a maximum depth of 2.5 mm in the z-plane. The OCT acquisition and the excitation of the 5 MHz transducer were triggered by the computer controlling the entire process.

The PhS-OCT characteristics include a full-width half-maximum (FWHM) bandwidth of 125 nm, and a light source frequency sweep rate of 20 kHz. The maximum sensitivity of the system was measured to be 112 dB.[25] The imaging depth of the system was measured to be 5 mm in air (-10 dB sensitive fall-off). The optical lateral point spread function was approximately 30 μm, and the FWHM of the axial point spread function after dispersion compensation was 10 μm. The synchronized control of the galvanometer and the OCT data acquisition was conducted through a LabVIEW platform (National Instruments, Austin, TX, USA) connected to a workstation. The phase stability of the system was calculated as the standard deviation of the temporal fluctuations of the Doppler phase-shift ($\Delta\phi_{err}$) while imaging a static structure.[26] Results show $\Delta\phi_{err} = 4.6$ mrad when using Loupas' algorithm.[27] The displacement sensitivity is measured as the minimum detectable axial particle displacement ($u_{z,\min}$). We found $u_{z,\min} = 0.358$ nm. Finally, the maximum axial displacement supported by the system without unwrapping the phase-shift signal ($\Delta\phi_{\max} = \pi$) is $u_{z,\max} = 0.24$ μm.

3.2 Sample preparation and measurement

Two tissue-mimicking phantoms where used in experiments. A cylindrically-shaped custom shear wave viscoelastic phantom (model no. 16410001, CIRS, Norfolk, VA, USA) was used as dispersive medium (5.4 cm in diameter $\times$ 2.2 cm in height). A cylindrically-shaped aqueous elastic phantom (Aquaflex US del pad, Parker Laboratories INC., Fairfield, NJ, USA) was selected as the elastic medium (9 cm in diameter $\times$ 2 cm in height). The frequency-dependent Young's modulus of each phantom was measured using a stress-relaxation by compression test. The measurement was conducted using a MTS Q-Test/5 Universal Testing Machine (MTS, Eden Prairie, MN, USA) with a 5 N load cell using a compression rate of 0.5 mm/s, a strain value of 5%, and total measurement time of 600 s. The stress-time plots obtained by the machine were fitted to a three parameter Kelvin-Voigt fractional derivative (KVFD) model[28] for the calculation of frequency-dependent complex Young's modulus. For both phantoms, the density was considered $\rho = 1$ g/cm^3. The three estimated parameters of the KVFD model are detailed in Table 1.

Table 1. Mechanical testing results in elastic and viscoelastic phantoms. Kelvin-Voigt fractional derivative parameters (left col.) and compression test results (right col.) are shown for both media. Quasi-static shear wave speed was calculated using $c(\omega \approx 0) = Real\{\sqrt{E^*/(3\rho)}\}$ for $\rho = 1$ g/cm^3 and assuming incompressibility. All experiments were performed at room temperature (25 °C).

	Stress relaxation test: Kelvin-Voigt fractional derivative model parameters			Quasi-static compression test: Young's modulus and shear speed	
	E_0 (kPa)	η (kPa s^α)	τ	$E(\omega \approx 0)$	$c(\omega \approx 0)$
Viscoelastic phantom	0.711 ± 0.481	5.203 ± 0.852	0.178 ± 0.028	4.98 ± 0.24	1.29 ± 0.02
Elastic phantom	9.969 ± 9.661	24.928 ± 12.217	0.086 ± 0.025	34.51 ± 0.85	3.39 ± 0.04

Finally, we investigate the feasibility of using the proposed general propagation model approach for quantifying the viscoelastic properties of collagen hydrogels in tissue engineering environments. A previous study demonstrated that measurement of stiffness of collagen gels using SWEI can be complicated by the presence of Scholte waves.[29] Collagen solutions were prepared on ice by combining in order 10X phosphate buffered saline (PBS), Type I collagen (Corning, Type I rat tail collagen), and 1 X PBS. Sodium hydroxide was added to adjust the pH to 6.8-10. Collagen solutions were degassed on ice for 40 minutes at 18 psi. After pipetting collagen solution into 1 cm diameter wells within a 6-well plate modified with elastomer molds, the hydrogels polymerized in an incubator (37 °C, 8% CO$_2$) for at least one hour. Polymerized hydrogels contained collagen concentrations of 2 mg/mL and 5 mg/mL.

Collagen hydrogels with starting concentrations of 2 mg/mL and 5 mg/mL were dehydrated to concentrations of 6.7 mg/mL and 10.6 mg/mL, respectively. PBS was removed from the polymerized hydrogel using rolled Kimwipes. The net mass of PBS removed from the hydrogel was determined by computing the difference in mass between the wet and dry Kimwipe on a weigh boat. We assumed no collagen was removed, and the mass of collagen and remaining volume of PBS in the hydrogel was used to calculate the dehydrated collagen concentration.

After fabrication, collagen hydrogels were removed from the wells and placed on top of a holder covered with a Saran membrane, which was partially submerged in a tank of saline water coupling the ultrasonic transducer to the sample. The Saran membrane separated the collagen hydrogel from the water, and provided an acoustic propagation path with reduced reflections. The ARF push was focused at the center of the outer surface of all collagen gels to ensure cylindrical wave propagation.

3.3 Acquisition and processing

Due to speed limitations of the OCT acquisition system, a complete phase front of a single ARF excitation cannot be instantly acquired within a ROI. Therefore, a repeated excitation/acquisition triggered at any single spatial location within the ROI is conducted. This method, also called the M-B mode acquisition protocol, is described in Zvietcovich et al.[5]

The repeated acquisition and ARF excitation are possible since they are synchronized with the same cyclic trigger signal of 7 ms periodicity. The ARF tone is formed by 5000 cycles of a 5 MHz harmonic wave equivalent to a 1 ms excitation. The M-B mode approach is used for generating x-axis space-time representations of particle velocity $v_z(z)$ at a given z_0 and y_0 position. In this study, we constrained the analysis to the surface of the sample so that z_0 corresponds to the axial position of surface for any (x_0, y_0) location. Each M-B acquisition spans 200 locations in the x-axis (10 mm), and $M = 100$ time samples (5 ms) as shown in Figure 2. Then, we repeat this process at each location y_0 in the y-axis for 200 positions (10 mm). In total, we acquired a 3D matrix volume of 200 ×200 ×100 measurements of $v_z(z_0)$ in the x, y, and time axes, respectively, using the described protocol in order to cover the ROI of 10 ×10 mm at z_0, and 5 ms in the time frame. Each profile cut of the 3D matrix in the xy-plane corresponds to a motion frame at a frame rate of 20 kHz (time resolution Δ_M=50 μs). The total acquisition time was 4.6 min.

Without loss of generality, we can call the 3D matrix representing particle velocity at the surface of the sample $v_{z_0}(x, y, t)$, where x and y represent spatial coordinates on the surface, and t is the time domain. We want to fit the analytical model of Equation 5 ($\hat{v}(r, \omega)$) to the data in $v_{z_0}(x, y, t)$, however, $\hat{v}(r, \omega)$ is defined in the cylindrical r-axis.
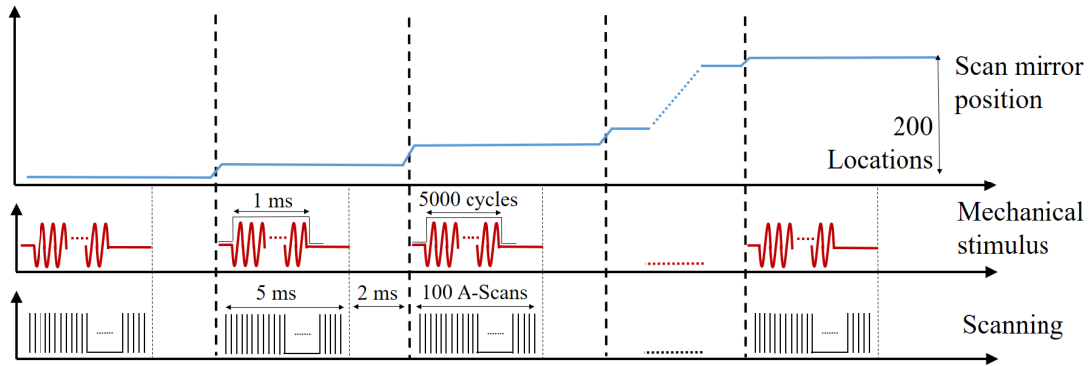
Figure 2. M-B mode acquisition protocol of motion signals using a PhS-OCT system.

Therefore, taking a profile cut of $v_{z_0}(x, y, t)$ along the xy-plane containing the center of the ARF excitation, and cropping the data to achieve a one-sided propagation matrix, we obtain $v_{z_0}(r, t)$. Taking $\hat{v}_{z_0}(r, \omega) = \mathfrak{I}\{v_{z_0}(r, t)\}$, and deriving A_0 in Equation 5 by normalizing the data with the model for the maximum peak value, we can solve
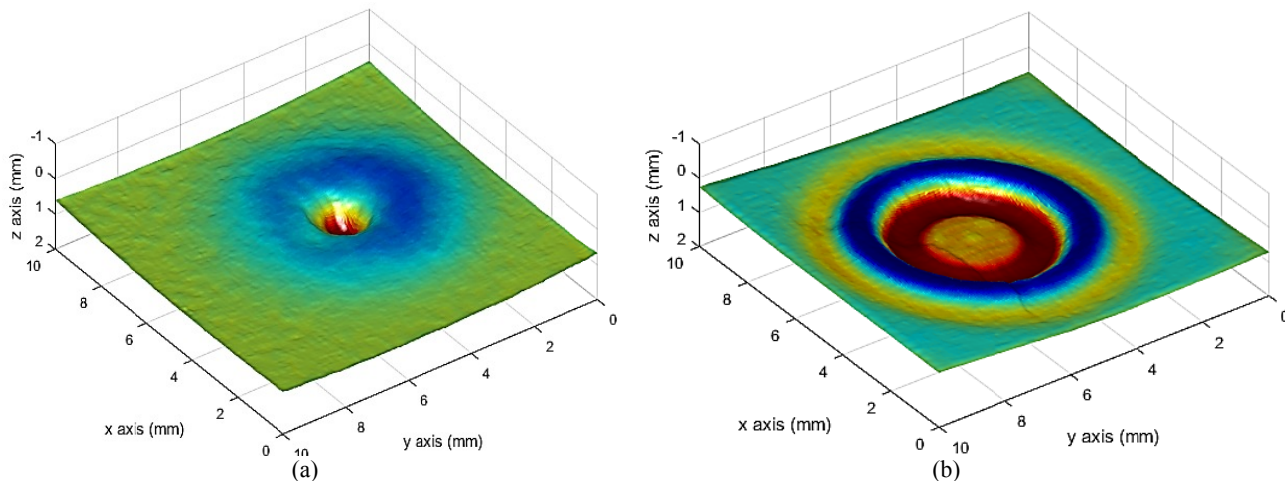
$$\{c_0^*, c_1^*, \alpha_1^*\} = \underset{c_0, c_1, \alpha_1}{\arg\min} \left\| |\hat{v}(r, \omega)| - |\hat{v}_{z_0}(r, \omega)| \right\|_2^2 \qquad (10)$$

for the unknown parameters c_0, c_1, and α_1. Equation 10 is a non-linear least squares problem and we employ the Levenberg-Marquardt method[30] for generating a solution.

4. RESULTS

4.1 Phantom experiments

Video 1 shows the wave propagation of the Gaussian-shaped pulse in the viscoelastic and elastic phantoms, and Figure 3 shows particle velocity frames $v_{z_0}(x, y; \{t_0, t_1, t_2\})$ for three different time instants extracted at the surface of each phantom as described in Section 3.3. We defined the initial time $t = 0$ s at the falling edge of the ARF pulse. The ARF push location is found to be approximately at the center of the ROI. The cylindrical spreading of the wave when traveling out of the source is evident in both cases. The attenuation of the peak is more pronounced in the viscoelastic case when compared to the elastic case, as expected.

Video 1. Wave propagation videos of a Gaussian-shaped pulse in (a) viscoelastic and (b) elastic phantoms. Videos available at http://dx.doi.org/10.1117/12.2287553.1
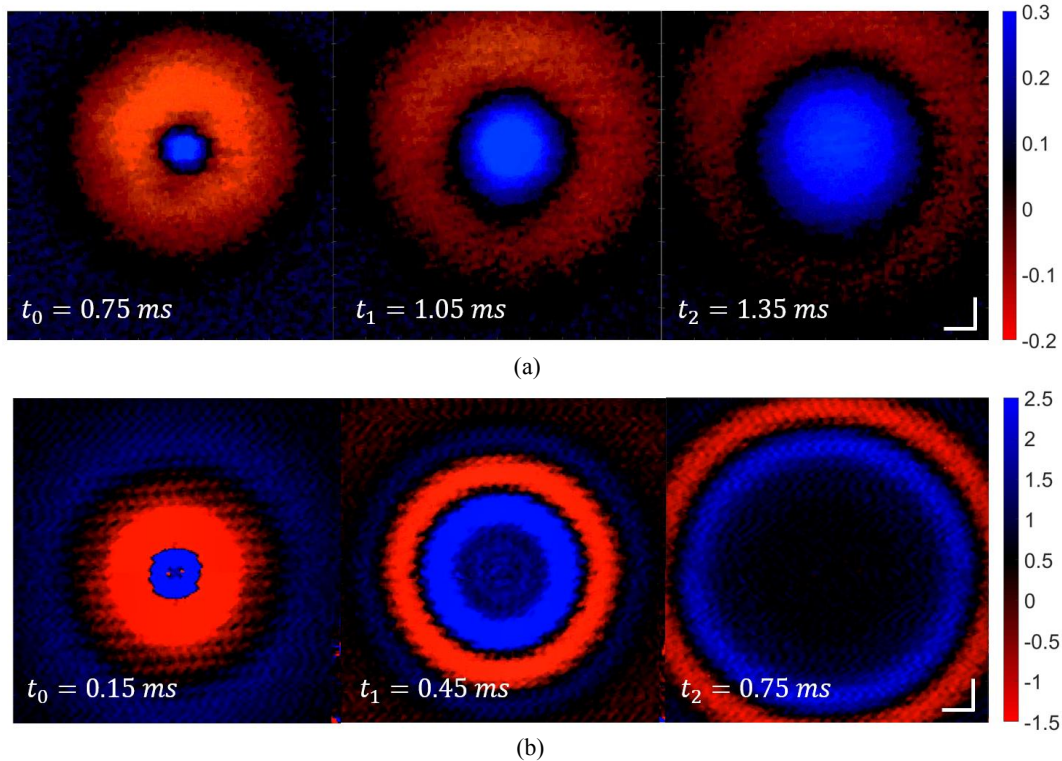
Figure 3. Motion snapshots of cylindrical wave propagation at different instants for (a) viscoelastic and (b) elastic phantoms. Color bar scale is in radians related to the OCT Doppler phase-shift caused by particle motion in phantoms. White spatial scale reference: 1 mm.

Profile cuts in the *x*-direction centered to contain the ARF excitation origin were obtained from $v_{z_0}(x, y, t)$ in the viscoelastic and elastic cases and are shown in Figures 4a and 4b, respectively. A Gaussian bell shape is initially observed at the first instant. After solving Equation 10, results are shown in Table 2. In addition, parameter *a* in the rectangular function of the application function $T(t)$ is set to be $a = 1$ ms. Figures 4c and 4d show $\left|\hat{v}_{z_0}(r, \omega)\right|$ plots for the viscoelastic and elastic cases, respectively. The appearance of the sinc function in the frequency axis confirms the validity of $\hat{T}(\omega)$ in Equation 4. Moreover, the attenuation of the main lobe in $\left|\hat{v}_{z_0}(r, \omega)\right|$ for the viscoelastic case tends to move the peak towards smaller values of frequency as *r* increases, which makes evident the presence of a frequency-dependent attenuation attributed to α_1. In contrast, this behavior is not strong for the elastic case, as expected.

Table 2. Estimation of optimized parameters $\{c_0^*, c_1^*, \alpha_1^*\}$ using the Levenberg-Marquardt inversion method for solving Equation 10 in experiments with phantoms and porcine cornea tissue.

	c_0^* (m/s)	c_1^* (m/s/Hz)	α_1^* (NP/mm/kHz)
Viscoelastic phantom	2.88 ± 0.03	$9.75*10^{-7} \pm 0.87*10^{-7}$	0.049 ± 0.001
Elastic phantom	4.61 ± 0.02	$2.58*10^{-7} \pm 0.14*10^{-7}$	0.0098 ± 0.0005

The Levenberg-Marquardt method was applied to Equation 10 for different initial values of $\{c_0, c_1, \alpha_1\}$, and we found convergent solutions for the viscoelastic and elastic cases, as reported in Table 2. Equation 5 is mesh plotted in the $f - r$ space using the optimized parameters $\{c_0^*, c_1^*, \alpha_1^*\}$ in Figures 4c and 4d for the viscoelastic and elastic cases, respectively. Given the results of mechanical testing in Table 1, we plotted the real and imaginary parts of the wavenumber as a function of frequency in Figure 5, and we compared them with the components of the complex wavenumber obtained using results in Table 2 and Equation 7. We found good agreement of our model within the boundaries of the mechanical testing results for the viscoelastic and elastic cases. It is also evident that α_1^* for the viscoelastic case is half an order of magnitude higher compared to the elastic one, which was expected.
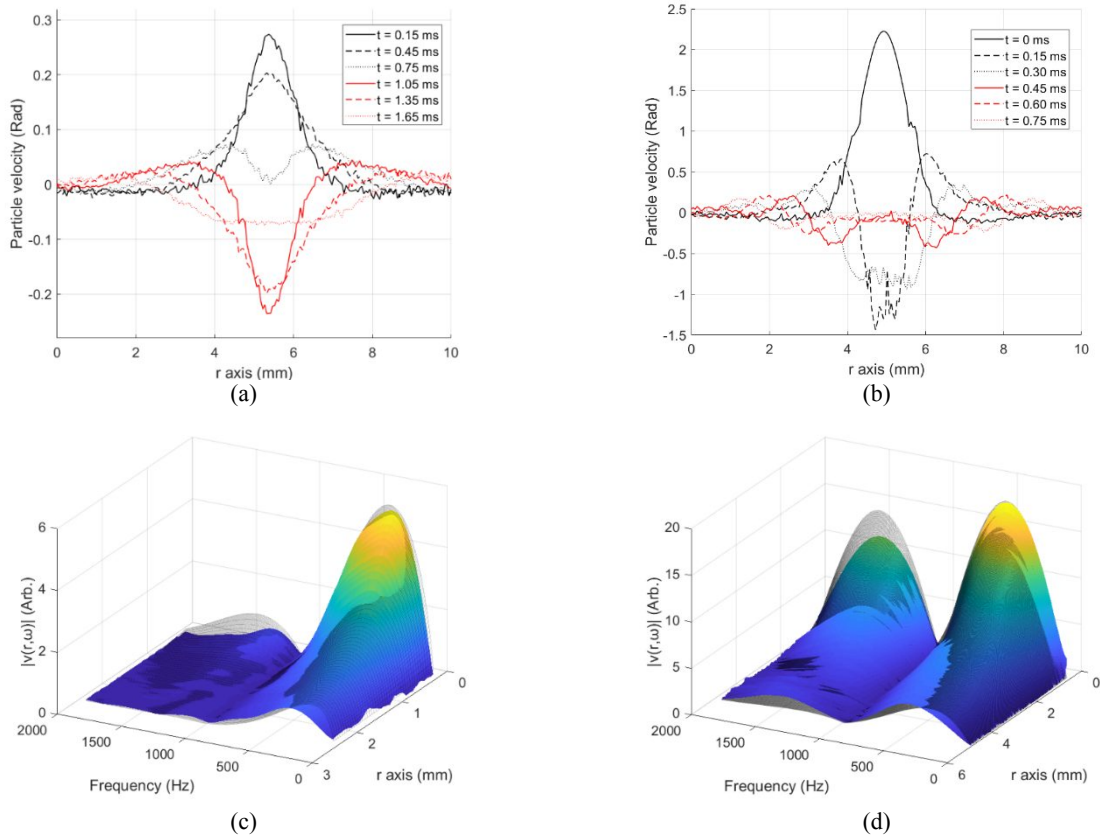
(a)

(b)

(c)

(d)

Figure 4. Experimental plots of $v_{z_0}(x, y, t)$ (top row), and $\left|\hat{v}_{z_0}(r, \omega)\right|$ (bottom row) for a viscoelastic (a, c) and elastic (b, d) media. $\omega = 2\pi f$, and f = frequency. For all cases, the input force has an approximate Gaussian shape, and $a = 1$ ms. Black mesh in (c, d) shows $|\hat{v}(r, \omega)|$ for the optimized parameters $\{c_0^*, c_1^*, \alpha_1^*\}$ using the Levenberg-Marquardt inversion method. Particle velocity units are show in radians referring to the OCT Doppler phase-shift.
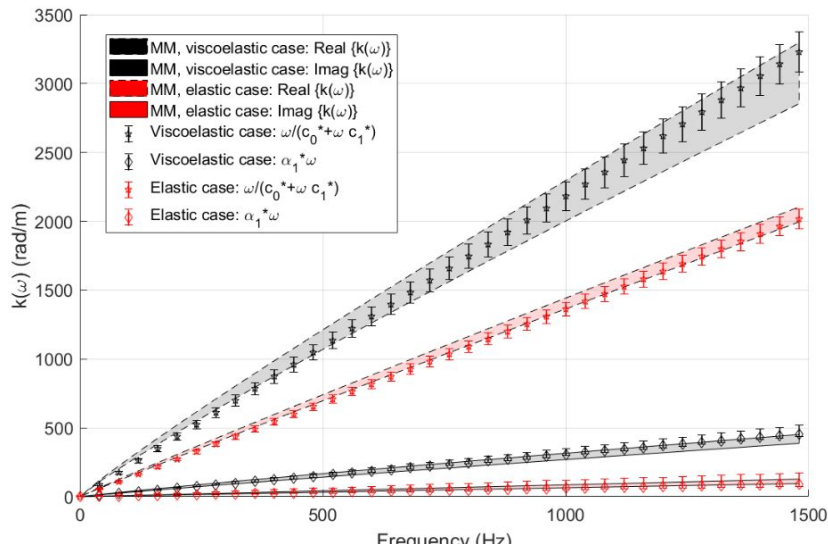

Figure 5. Frequency-dependent wavenumber comparison between mechanical measurements (MM) results using the KVFD model and our general propagation model (using optimized parameters $\{c_0^*, c_1^*, \alpha_1^*\}$). $\omega = 2\pi f$, and f = frequency. The real and imaginary part of the wavenumber are plotted as a function of frequency for the viscoelastic and elastic phantoms.

4.2 Collagen hydrogels

Collagen is the predominant structural protein in a wide range of tissues, and therefore can serve as a versatile scaffold for a variety of tissue engineering applications[31]. The mechanical properties of engineered scaffold materials can influence cellular behaviors such as migration and multicellular organization, and can predict how an engineered tissue will respond to physiological loading conditions once implanted in the body[32,33,34]. Furthermore, cells are capable of modifying their environment through processes such as extracellular matrix deposition, contraction, and protease degradation, and these behaviors may influence the properties of a biological material over time[35,36]. Mechanical testing can measure viscoelastic properties, but these techniques are destructive to the developing engineered tissues. Therefore, innovating non-invasive, non-destructive technologies to quantify viscoelastic parameters is essential for longitudinal monitoring of engineered tissue constructs.

Results from an exploratory study are shown in Figure 6. The figure shows the shear speed parameter c_0^*, and the attenuation coefficient α_1^* for the four collagen hydrogel concentrations. c_0^* shows a decreasing tendency for the first three samples when concentration increases. However, the last sample concentration has the maximum c_0^* result. Values of the attenuation coefficient are more consistent as they increase with the concentration for all cases, indicating a potential relationship to collagen microstructure. Future work will concentrate on the validation of this technique in collagen hydrogels since it holds potential as a non-destructive, non-invasive tool to evaluate the mechanical properties of engineered tissues during their fabrication and development.
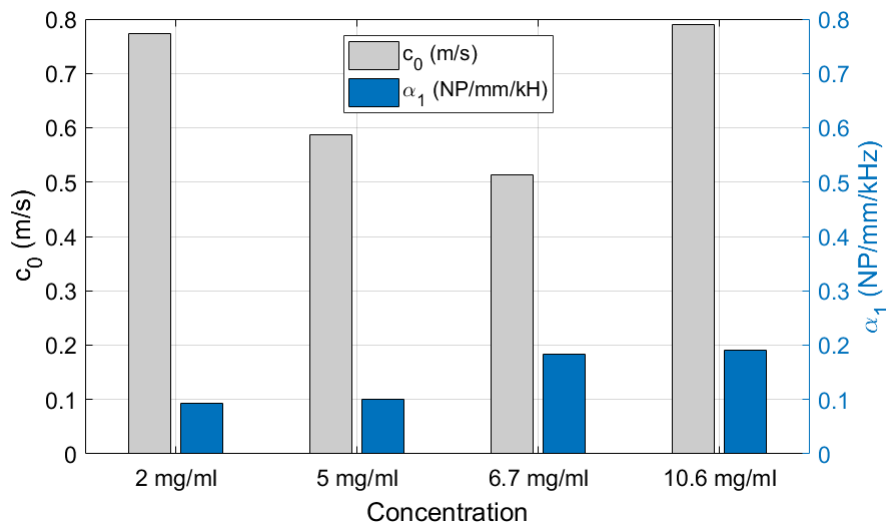

Figure 6. Shear speed c_0^* (left axis) and attenuation α_1^* (right axis) calculated from collagen hydrogels at different concentrations using our general propagation model. Parameter c_1^* was found to be negligible for all cases and not significant for further comparison.

5. CONCLUSION

The application of an analytical general cylindrical wave propagation model for the viscoelastic characterization of dispersive media has been demonstrated. Experimental results in elastic and viscoelastic phantoms support the effectiveness of the approach when compared to mechanical testing results. Our proposed model of propagation takes into account (1) the initial force shape of the excitation pulse in the space-time field, (2) wave speed dispersion, (3) wave attenuation caused by material properties of the sample, (4) wave spreading caused by the outward cylindrical propagation of the wavefronts, and (5) the rheological-independent estimation of the dispersive medium. The model is versatile enough to be tuned with any type of input push-force produced by the desired excitation method. Moreover, in contrast to the majority of approaches that use only the frequency-dependent wave speed data for the calculation of viscoelastic parameters using a rheological model, our approach utilizes the wave attenuation data, which is fundamental

for the accurate viscoelastic characterization of the sample without assuming any rheological model. This last advantage is significant for the study of tissue with unknown mechanical behavior. Finally, wave propagation in collagen hydrogels was analyzed and compensated for cylindrical spreading using this approach. Viscoelastic parameters of the hydrogels were calculated and compared to their concentrations. Future work will extend this research to a general Lamb wave model using different rheological models for the accurate estimation of viscous parameters in other tissues such as porcine and human cornea.

REFERENCES

[1] Parker, K. J., Doyley, M. M., and Rubens, D. J., "Imaging the elastic properties of tissue: the 20 year perspective," Physics in Medicine and Biology **56**(1), R1 (2011).

[2] Schmitt, C., Soulez, C., Maurice, G., Giroux, M. F., and Cloutier, G., "Noninvasive vascular elastography: toward a complementary characterization tool of atherosclerosis in carotid arteries," Ultrasound in Medicine & Biology **33**(12), 1841-1858 (2007).

[3] Mulligan, J. A., Untracht, G. R., Chandrasekaran, S. N., Brown, C. N., and Adie, S. G., "Emerging approaches for high-resolution imaging of tissue biomechanics with optical coherence elastography," Selected Topics in Quantum Electronics, IEEE Journal of **22**(3), 1-20 (2016).

[4] Drexler, W., Liu, M., Kumar, A., Kamali, T., Unterhuber, A., and Leitgeb R. A., "Optical coherence tomography today: speed, contrast, and multimodality," Journal of Biomedical Optics **19**(7), 071412-071412 (2014).

[5] Zvietcovich, F., Rolland, J. P., Yao, J., Meemon, P., and Parker, K. J., "Comparative study of shear wave-based elastography techniques in optical coherence tomography," Journal of Biomedical Optics **22**(3), 035010-035010 (2017).

[6] Larin, K. V., and Sampson, D. D., "Optical coherence elastography - OCT at work in tissue biomechanics [Invited]," Biomed. Opt. Express **8**(2), 1172-1202 (2017).

[7] Parker, K. J., and Baddour, N., "The Gaussian Shear Wave in a Dispersive Medium," Ultrasound in medicine & biology **40**(4), 675-684 (2014).

[8] Garteiser P., Doblas, S., Daire, J. L., Wagner, M., Leitao, H., Vilgrain, V., Sinkus, R., and Van Beers, B. E., "MR elastography of liver tumours: value of viscoelastic properties for tumour characterisation," European Radiology **22**(10), 2169-2177 (2012).

[9] Streitberger K-J., Reiss-Zimmermann, M., Freiman, F. B., Bayerl, S., Guo, J., Arlt, F., Wuerfel, J., Braun, J., Hoffman, K-T., and Sack, I., "High-Resolution Mechanical Imaging of Glioblastoma by Multifrequency Magnetic Resonance Elastography," PLOS ONE **9**(10), e110588 (2014).

[10] Han, Z., Singh, M., Aglyamov, S. R., Liu, C. H., Nair, A., Raghunathan, R., Wu, C., Li, J., and Larin, K. V.,"Quantifying tissue viscoelasticity using optical coherence elastography and the Rayleigh wave model," Journal of Biomedical Optics **21**(9), 090504-090504 (2016).

[11] Zhang X., "Identification of the Rayleigh surface waves for estimation of viscoelasticity using the surface wave elastography technique," The Journal of the Acoustical Society of America **140**(5), 3619-3622 (2016).

[12] Han, Z., Li, J., Singh, M., Wu, C., Liu, C. H., Raghunathan, R., Aglyamov, S. R., Vantipalli, S., Twa, M. D., and Larin, K. V., "Optical coherence elastography assessment of corneal viscoelasticity with a modified Rayleigh-Lamb wave model," Journal of the Mechanical Behavior of Biomedical Materials **66**(87-94 (2017).

[13] Wijesinghe P., McLaughlin, R. A., Sampson, D. D., and Kennedy, B. F., "Parametric imaging of viscoelasticity using optical coherence elastography," Physics in Medicine & Biology **60**(6), 2293 (2015).

[14] Schmitt, C., Hadj Henni, A., and Cloutier, G., "Ultrasound Dynamic Micro-Elastography Applied to the Viscoelastic Characterization of Soft Tissues and Arterial Walls," Ultrasound in Medicine and Biology **36**(9), 1492-1503 (2010).

[15] Nenadic I. Z., Qiang, B., Urban, M. W., Zhao, H., Sanchez, W., Greenleaf, J. F., and Chen, S., "Attenuation measuring ultrasound shearwave elastography and in vivo application in post-transplant liver patients," Physics in Medicine & Biology **62**(2), 484 (2017).

[16] Kazemirad S., Bernard, S., Hybois, S., Tang, A., and Cloutier, G., "Ultrasound Shear Wave Viscoelastography: Model-Independent Quantification of the Complex Shear Modulus," IEEE Transactions on Ultrasonics, Ferroelectrics, and Frequency Control **63**(9), 1399-1408 (2016).

[17] Leartprapun, N., Iyer, R., Adie, S. G., "Model-independent quantification of soft tissue viscoelasticity with dynamic optical coherence elastography", Proc. SPIE 10053, Optical Coherence Tomography and Coherence Domain Optical Methods in Biomedicine XXI, 1005322 (17 February 2017)

[18] Zvietcovich, F., Rolland, J. P., and Parker, K. J., "An approach to viscoelastic characterization of dispersive media by inversion of a general wave propagation model," J. Innov. Opt. Health Sci. 10, 1742008 (2017).

[19] Graff, K. F., [Wave motion in elastic solids], Dover Publications, 283-288 (2012)

[20] Baddour, N., "Multidimensional wave field signal theory: Mathematical foundations," AIP Advances **1**(2), 022120 (2011).

[21] Carstensen, E. L., and Parker, K. J., "Physical Models of Tissue in Shear Fields - This article is dedicated to our friend and colleague, Robert C. Waag," Ultrasound in Medicine & Biology **40**(4), 655-674 (2014).

[22] Zvietcovich, F., Yao, J., Rolland, J. P., and Parker, K. J., "Experimental classification of surface waves in optical coherence elastography," in Optical Elastography and Tissue Biomechanics III, K. V. Larin, D.D. Sampson, Ed., Proc. SPIE **9710**, 97100Z (2016) [doi:10.1117/12.2211420].

[23] Viktorov, I. A., [Rayleigh and Lamb Waves: Physical Theory and Applications], Springer, US, ch 1 (2013).

[24] Abramowitz, M., and Stegun, I, A., [Handbook of Mathematical Functions: with Formulas, Graphs, and Mathematical Tables], Dover Publications, (2012).

[25] Yao, J., Panomsak, M., Ponting, M., and Rolland, J. P., "Angular scan optical coherence tomography imaging and metrology of spherical gradient refractive index preforms," Optics Express **23**(5), 6428-6443 (2015).

[26] Meemon, P., Lee, K., and Rolland, J. P., "Doppler imaging with dual-detection full-range frequency domain optical coherence tomography," Biomedical Optics Express **1**(2), 537-552 (2010).

[27] Loupas, T., Peterson, R. B., and Gill, R. W., "Experimental evaluation of velocity and power estimation for ultrasound blood flow imaging, by means of a two-dimensional autocorrelation approach," Ultrasonics, Ferroelectrics, and Frequency Control, IEEE Transactions on **42**(4), 689-699 (1995).

[28] Zhang, M., Nigwekar, P., Castaneda, B., Hoyt, K., Joseph, J. V., di Sant'Agnese, A., Messing, E. M., Strang, J. G., Rubens, D. J., and Parker, K. J., "Quantitative Characterization of Viscoelastic Properties of Human Prostate Correlated with Histology," Ultrasound in Medicine & Biology **34**(7), 1033-1042 (2008).

[29] Mercado, K. P., Langdon, J., Helguera, M., McAleavey, S. A., Hocking, D. C., and Dalecki, D., "Scholte wave generation during single tracking location shear wave elasticity imaging of engineered tissues," J Acoustic Soc Am Express Letters **138**(2), 138-144 (2015).

[30] Moré, J. J., "The Levenberg-Marquardt algorithm: Implementation and theory," in Numerical Analysis: Proceedings of the Biennial Conference Held at Dundee, June 28–July 1, 1977 G. A. Watson, Ed., pp. 105-116, Springer Berlin Heidelberg, Berlin, Heidelberg (1978).

[31] Parenteau-Bareil, R., Gavin, R., and Berthod, F., "Collagen-based biomaterials for tissue engineering applications," Materials **3**, 1863-1887 (2010).

[32] Hadjipanayi, E., Mudera, V., and Brown, R.A., "Guiding cell migration in 3D: A collagen matrix with graded directional stiffness, Cell Motility and the Cytoskeleton **66**,121-128 (2009).

[33] Mason, B.N., Starchenko, A., Williams, R.M., Bonassar, L.J., Reinhart-King, C.A., "Tuning three-dimensional collagen matrix stiffness independently of collagen concentration modulates endothelial cell behavior," Acta Biomaterialia **9**, 4635-4644 (2013).

[34] Inzana, J.A., Olvera, D., Fuller, S.M., Kelly, J.P., Graeve, O.A., Schwarz, E.M., Kates, S.L., and Awad, H.A., "3D printing of composite calcium phosphate and collagen scaffolds for bone regeneration," Biomaterials **35**(13), 4026-4034 (2014).

[35] Gildner, C.D., Lerner, A.L., and Hocking, D.C., "Fibronectin matrix polymerization increases tensile strength of model tissue," American Journal of Physiology, Heart Circulation Physiology **287**, H46-H53 (2004).

[36] Lu, P., Takai, K., Weaver, V.M., and Werb, Z., "Extracellular matrix degradation and remodeling in development and disease," Coldspring Harbor Perspectives in Biology **3**, a005058 (2011).